Design and tests of the prototype beam monitor of the CSR external target experiment

Hu-Lin Wang[1,2] · Zhen Wang[3] · Chao-Song Gao[1,2] · Jian-Wei Liao[4] ·
Xiang-Ming Sun[1,2] · Hai-Bo Yang[4] · Cheng-Xin Zhao[4] · Jun Liu[1,2] ·
Peng Ma[4] · Zi-Li Li[1,2] · Bi-Hui You[1,2] · Ping Yang[1,2] · Di Guo[1,2] · Le Xiao[1,2] ·
Dong-Liang Zhang[1,2] · Yue-Zhao Zhang[4] · Sheng Dong[1,2] · Wan-Han Feng[1,2] ·
Yu-Xin Qiao[1,2] · Zheng-Yu Hu[1,2] · Qing-Wen Ye[1,2] · Zeng-Tao Guo[1,2] ·
Guang-Ming Huang[1,2] · Feng Liu[1,2]

Abstract A prototype beam monitor was designed to provide tracking information for heavy-ion projectiles for the cool storage ring (CSR) external target experiment (CEE) at the Heavy Ion Research Facility in Lanzhou (HIRFL). High granularity and direct charge sensing are the main features of this device. It measures the beam position in a two-dimensional (2D) plane transverse to the beam direction on an event-by-event basis. The current design consists of two field cages inside a single vessel that operates independently and has electrical drift fields in orthogonal directions. Preliminary tests of the prototype were performed using a ^{241}Am α source. The results show that a spatial resolution of less than 40 μm and a time resolution of less than 600 ns can be achieved.

Keywords CEE · Beam monitor · Heavy ion · Topmetal sensor · Tracking · Field cage

✉ Zhen Wang
kathwz@163.com

✉ Chao-Song Gao
chaosonggao@ccnu.edu.cn

1 PLAC, Key Laboratory of Quark and Lepton Physics (MOE), Central China Normal University, Wuhan 430079, China

2 Hubei Provincial Engineering Research Center of Silicon Pixel Chip & Detection Technology, Wuhan 430079, China

3 School of Physics and Electronic Science, Guizhou Normal University, Guiyang 550001, China

4 Institute of Modern Physics, Chinese Academy of Sciences, Lanzhou 730000, China

1 Introduction

The CEE spectrometer [1] will be the first large-scale nuclear physics experiment device to study heavy-ion collisions at the CSR of HIRFL [2–4]. The HIRFL-CSR can deliver heavy ion beams of elements from carbon to uranium and energies up to 1 GeV/u. The physics program at the CEE requires a beam monitor system to track the beam particles with rates up to 1 MHz on an event-by-event basis to monitor the beam profile and aid in reconstructing the primary collision vertex. As depicted in Fig. 1, the CEE detector system consists of a dipole magnet, tracking system, time-of-flight (TOF) system [5–7], and zero-degree calorimeter (ZDC) [8]. The tracking system includes a time projection chamber (TPC) [9, 10], multiwire drift chambers (MWDCs) [11–14], and beam monitoring.

The main requirements of CEE on the beam monitor are:

- spatial resolution of less than 50 μm;
- time resolution of less than 1 μs;
- minimum interference with the beam.

One of the main challenges is that all the components of the beam monitor have long-term stability and are resilient to aging in an environment with a high level of radiation. Another main challenge is that it must work in a non-uniform magnetic field of approximately a few hundred gauss, which is foreseeable inside the magnetic shield close to the collision point without much deterioration of the performance.

To meet these stringent requirements, a prototype device utilizing two field cages with low-noise pixelated ASIC [15–17] was designed and assembled for charge
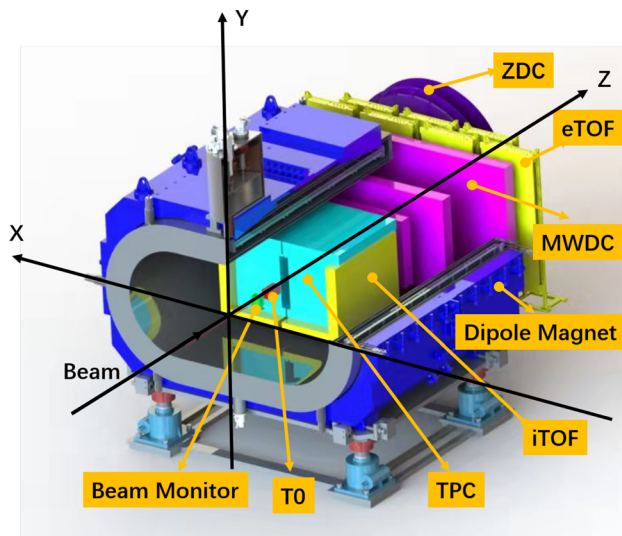
Fig. 1 (Color online) Schematic layout of the CEE spectrometer [1]

sensing and readout. Tests were carried out with injected signals and a ^{241}Am α source, with the preliminary evaluation showing promising results.

2 Design of the prototype

2.1 Field cage and vessel

The beam monitor is located at the beamline approximately a few tens of centimeters in front of the target. The beam direction is along the Z-axis as shown in Fig. 1. Figure 2 shows the basic structure of the beam monitor, which has a size of $120\,(X) \times 120\,(Y) \times 163\,(Z)$ mm^3. High-voltage connectors, gas inlet and outlet connectors, and readout electronics connectors were all led out through
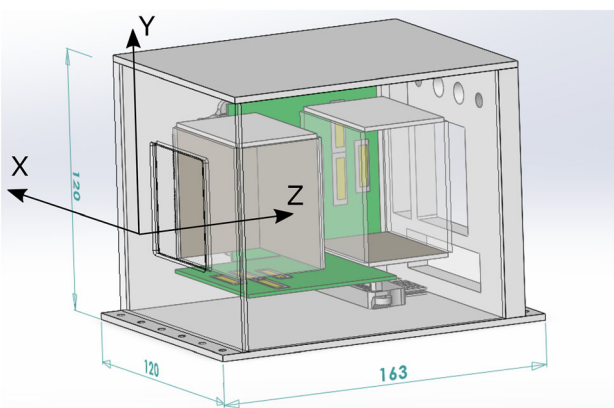

Fig. 2 (Color online) Basic structure of the beam monitor. The size of the beam monitor is $120\,(X) \times 120\,(Y) \times 163\,(Z)$ mm^3. Two cubic field cages are inside the gastight vessel. The yellow areas depict the low-noise pixelated chips acting as anodes

the X–Y plane on the vessel facing the positive Z-direction. Two cubic field cages were placed inside the vessel to provide a uniform electric field for drifting electrons. Each cage deploys low-noise pixelated ASICs named Topmetal [15–17], acting as the anode to detect drifting electrons. Two field cages operate independently and have electric drift fields in the orthogonal directions. As shown in Fig. 2, the drift field of one field cage is in the X-direction, whereas the Topmetal is on the Y–Z plane. The drift field of the other field cage is in the Y-direction, whereas the Topmetal is in the X–Z plane. The beam particle passes through the field cage along the z-axis, ionizing the gas along the path. The ionized electrons drift toward the Topmetal sensor under the influence of the electric field, sensed, and read out by the pixelated Topmetal sensor. The position of the beam particles can be calculated based on the signal distribution on the pixel array. The field cage with the Topmetal in the Y–Z plane provides the Y position of the beam, whereas the field cage with the Topmetal in the X–Z plane provides the X position of the beam. Therefore, both transverse coordinates of the beam particle can be measured.

The stringent requirement for position resolution makes the uniformity of the electric field an important factor; therefore, the field cages were carefully designed and simulated. To generate a uniform electric field, the field-cage structure commonly used in TPC was adopted [18]. The wall of the field cage is a Kapton foil carrying metal field strips. These field strips are parallel cubic rings that lie on potentials that incrementally fall from the anode toward the cathode at an even pace. The field strips ensure good drift field quality in the sensitive volume.

To determine the optimal layout of the field strips, electrostatic calculations with different geometries are performed using the finite element method. COMSOL Multiphysics [19] was used to build a simplified 2D model for its numerical solution, which contains the cathode, anode, field strips, and vessel, as shown in Fig. 3, respectively. The 2D model was adopted because it is much faster than the 3D model, and their difference is negligible for our application. The vessel and anode are set to be at ground potential. The voltage of the cathode is set to be at -2400 V. The distance between the cathode and anode is 80 mm. The gap between the electrodes and vessel is 10 mm. The pitch of the field strips was 2 mm, and the widths of the strips were set to 1 mm, 1.5 mm, and 1.8 mm, respectively, resulting in a gap between adjacent strips of 1 mm, 0.5 mm, and 0.2 mm, respectively. Figure 3 shows the distribution of the electric potential and electric field lines with a strip width of 1 mm. Owing to the ground potential of the vessel, the electric field lines diverge non-negligibly outward from the cathode to anode. The deviation between the starting and ending positions of
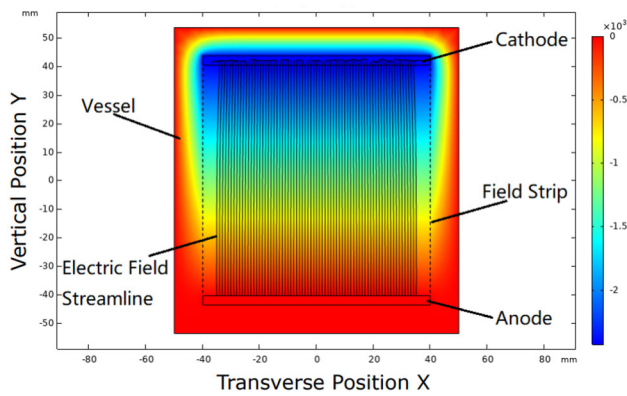
Fig. 3 (Color online) 2D COMSOL Model of one field cage for electric field calculation. The distribution of the electric potential and electric field lines is shown by a strip of 1 mm and a pitch of 2 mm. The sensitive volume of the field cage ranges from −15 to 15 mm in the X-axis

the electric field lines induces a bias on the reconstructed beam particle position, because the electrons drift macroscopically along the electric field lines in the gas. Figure 4 shows the shape of the electric field lines passing through
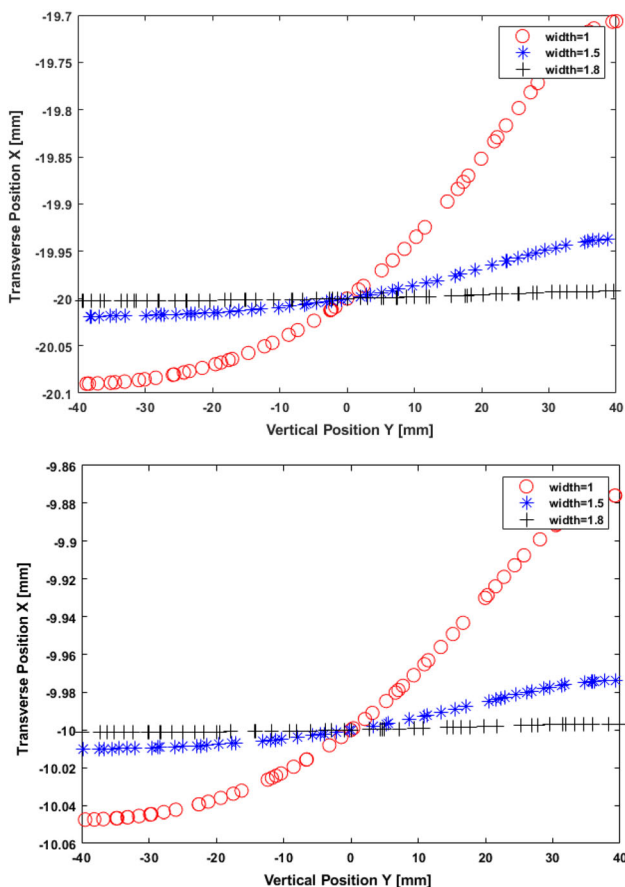
the point ($x = -20$ mm, $y = 0$) and ($x = -10$ m, $y = 0$) with strip widths of 1, 1.5 mm, and 1.8 mm, respectively. As shown in Fig. 4, the deviation between the starting and ending positions of the electric field lines decreases when the strip width increases while keeping the 2 mm pitch fixed. Figure 5 shows the maximum deviation between the starting and ending positions of the electric field lines with strip widths of 1, 1.5, and 1.8 mm and the ending positions at the anode and starting positions anywhere along the field lines. As shown in Fig. 5, the maximum deviation is less than 10 mm in the sensitive volume from −15 to 15 mm in the X-axis with a strip width of 1.8 mm and a pitch of 2 mm; this meets the requirement for the uniformity of the electric field and was chosen for our prototype design.

During assembly, the uncertainty of the resistance of each resistor in the chain and installation accuracy of the field strips both give rise to the distortion of the electric field. Therefore, their tolerance must be examined. To estimate the effect of the uncertainties of the resistors on the electric field, Gaussian random noise is added to the voltage of each field strip in the COMSOL simulation. The mean of the noise was set to 0, and the standard deviation was set to 60 V × $\sigma_{resistor}$. Here, 60 V is the nominal voltage difference between the adjacent field strips, and $\sigma_{resistor}$ was set to 1, 5, and 10%, respectively, representing the relative uncertainties of the resistors. The simulation results show that the 1% uncertainty meets the requirement. To estimate the impact of the installation accuracy of the field strips, Gaussian random noise was added to the position of each field strip in the COMSOL simulation. The mean of the noise was set to 0, and the standard deviation was set to 10 μm, 20 μm, and 50 μm, representing the installation accuracy of the field strips. The results show that the installation accuracy of field strips less than 20 μm satisfies the requirement of the beam monitor.
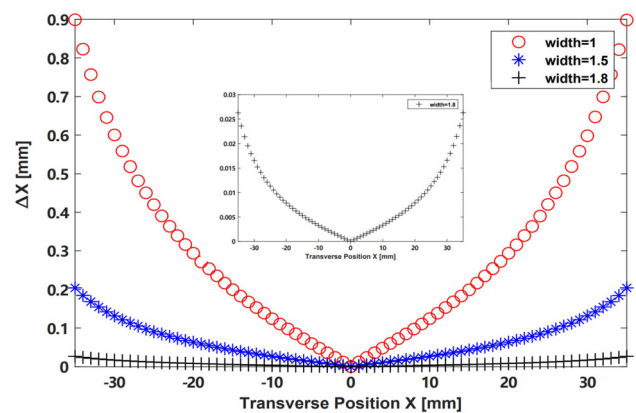

Fig. 4 Shape of the electric field lines passing through the point ($x = -20$ mm, $y = 0$) (top) and ($x = -10$ mm, $y = 0$) (bottom) with strip widths of 1 mm, 1.5 mm, and 1.8 mm, respectively

Fig. 5 Maximum deviation between the starting and ending positions of the electric field lines with the strip widths of 1, 1.5, and 1.8 mm. The ending positions are at the anode, and the starting positions are anywhere along the field lines

2.2 Charge sensing and readout chip

A charge-sensing and readout sensor, named Topmetal-CEE, has been specifically designed for beam monitoring and is currently under fabrication. Several Topmetal-CEE sensors are tiled on the bonding board, playing the role of the anodes of the field cage to sense drifting charges. The charge collecting principle of the Topmetal-CEE is shown in Fig. 6. The drifting charges are sensed by a piece of topmost metal exposed around the media, which is integrated into the silicon chip with the readout electronics.

The amplitude, position, and timing of the arriving charges can be recorded and read by the Topmetal-CEE sensor. The top structure of the Topmetal-CEE sensor is shown in Fig. 7. The Topmetal-CEE sensor is composed of three groups: an independent charge readout circuit, a high-speed transmission circuit, and a configuration circuit. In each charge readout circuit, ninety channels collect the charges independently. Subsequently, the hit information is read out using a data driver zero-compression priority readout circuit [20]. The analog signal is digitized using a 13-bit pipeline analog-to-digital converter (ADC) [21]. To sample the best amplitude of the analog signal, a 4-bit phase adjuster was designed to set the appropriate clock for the ADC. Because the data conversion time of the ADC requires five clock cycles, the 7-bit address and 8-bit counter values are also delayed by five clock cycles to match the timing. The high-speed transmission circuit consists of a frame builder, 8b/10b encoder, serializer, and phase-locked loop (PLL) [22]. The serializer features a data rate of 4.4 Gbps under a clock of 2.2 GHz provided by the PLL. The biases of the charge readout circuit are generated by digital-to-analog converters (DACs). The 16-bit input digital codes of each DAC are configured individually through a serial peripheral interface (SPI).
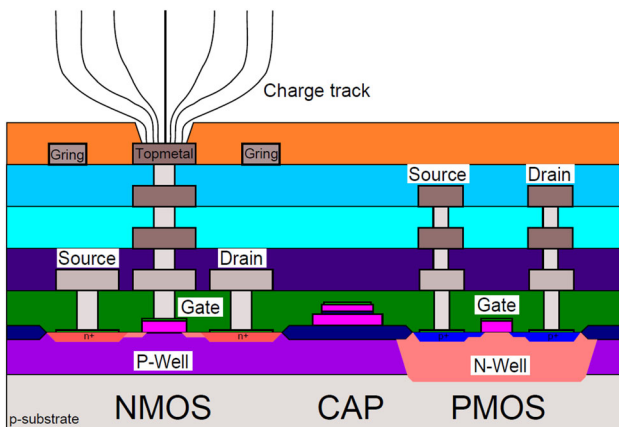

Fig. 6 (Color online) Principle of the charge collection of the Topmetal-CEE sensor
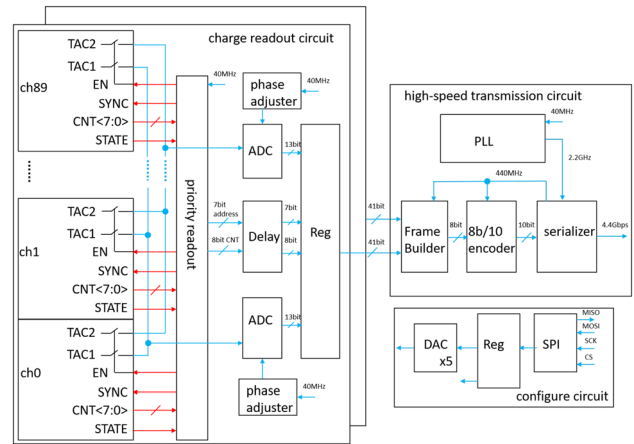

Fig. 7 Top structure of the Topmetal-CEE sensor

The structure of one channel of the Topmetal-CEE sensor is shown in Fig. 8. Each channel consists of a charge collection electrode (CCE), charge sensitive amplifier (CSA) [23], discriminator (DISCR), time-to-amplitude converter (TAC) [24], time-to-digital converter (TDC) [25], priority logic, and configuration module. The CCE is a topmost metal exposed in the media. The size of the CCE is 1 mm × 89 μm. A guard ring of the same metal surrounds the CCE, serving three purposes. First, it suppresses the cross talk between the readout pixels. Second, the 6 fF capacitance formed between the guard ring and CCE was used as the charge injection capacitor. Third, when a voltage lower than that of the CCE was applied to the guard ring, a focusing electrical field was formed, thereby improving the charge collection efficiency. The drifting charges in the field cage are sensed by the CCE and directly fed into the CSA. To increase the input dynamic range, the CSA can be configured to have different charge conversion gains by choosing feedback capacitors of 1, 20, and 100 fF in the feedback circuit, respectively. The output of the CSA is AC-coupled into the discriminator to avoid variations in the voltage of the baseline. Moreover, to reduce the mismatch between the different channels, the decay time of the CSA and threshold of the discriminator are both controlled by a global digital-to-analog converter (DAC) for coarse tuning and a local 6-bit DAC for fine-tuning. The TAC records the time over the threshold. The
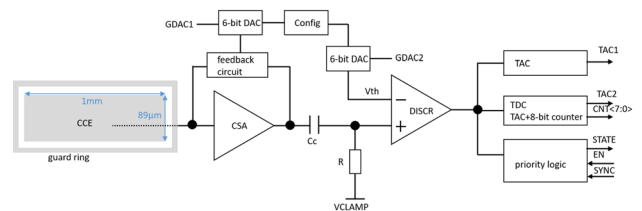

Fig. 8 Structure of one channel of the Topmetal-CEE sensor

time of arrival is recorded by the TDC. The priority logic decides when to read out the information.

The layout of the Topmetal-CEE is shown in Fig. 9. The total area is $19{,}038\,\mu m \times 4210\,\mu m$. The chip has been taped out and is under fabrication.

Here, the foundry is short of capacity, and the expected completion time of the fabrication of the Topmetal-CEE sensor has been delayed by a few months. Therefore, for the current prototype of the beam monitor, the Topmetal-II- sensor [16] in the Topmetal sensor family is used instead as the charge sensing and readout chip to demonstrate the working principle. Topmetal-II- was designed and fabricated during 2015–2016, sharing great similarities with Topmetal-CEE in terms of the charge sensing mechanism and CSA circuit. Therefore, the prototype of the beam monitor in the design phase utilizes the Topmetal-II- sensor, which will be upgraded to be based on the Topmetal-CEE sensor in the coming years in the next phase of the project.

The Topmetal-II- sensor includes both analog and digital readout schemes. However, for the digital readout scheme, the output of the CSA is directly fed into a comparator, that is, only a one-bit ADC is used. Therefore, the analog readout scheme of the Topmetal-II- sensor was chosen for the prototype beam monitor. The analog signal is transmitted off the chip and digitalized using a high-precision ADC. The principle of Topmetal-II- is thoroughly discussed in Ref. [16]; only a brief description of the analog readout scheme is presented herein. The structure of the analog readout scheme for Topmetal-II- is shown in Fig. 10. The Topmetal-II- sensor consists of a 72×72 pixel array with a pixel pitch of $83.2\,\mu m$, a scan module, and an analog buffer. The analog buffer is shared by all the pixels and transmits the analog signal from the chip, pixel by pixel (Fig. 11).

In the analog readout chain, the drifting charges are sensed by the CCE with an area of $25\,\mu m \times 25\,\mu m$ and then fed into the CSA directly. The CSA converts the current to voltage, and subsequently, the voltage is transmitted off the chip by a two-stage cascade source follower and a unit-gain buffer. The first-stage source follower isolates the interference from the switch (ROWSEL). The second-stage source follower drives the column-level bus, and driving
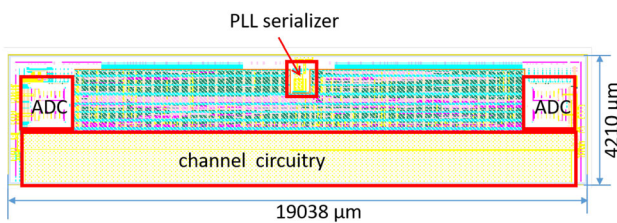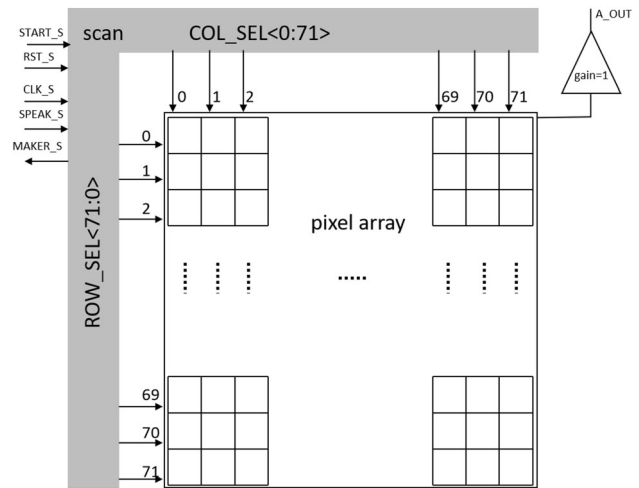
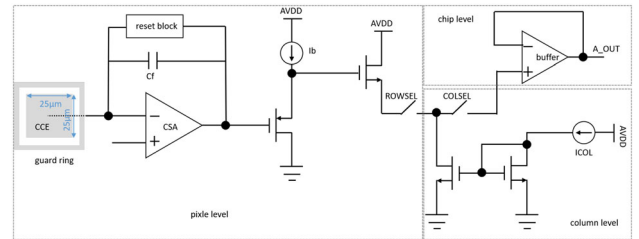**Fig. 10** Structure of the analog readout scheme of the Topmetal-II- sensor

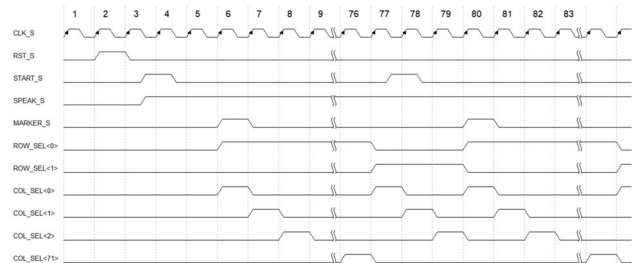**Fig. 11** Structure of the analog readout of each pixel in the Topmetal-II- sensor

Fig. 12 Readout timing of only scanning the first row

capacity can be tuned by adjusting the column-level current source (ICOL). The readout timing is shown in Fig. 12. First, a positive pulse of an asynchronous reset signal (RST_S) was applied to reset the state of the scan module. Second, a start pulse signal (START_S) is given, where the high level maintains a clock cycle. When START_S is flipped from a low level to a high level and SPEAK_S is at a high level, the first pixel is selected to be read out two clock cycles later. For example, in Fig. 12, START_S is flipped from a low to high level during the 77th and 78th clock cycles and the rising edge of the 78th clock cycle detected a high level of START_S when SPEAK_S was at
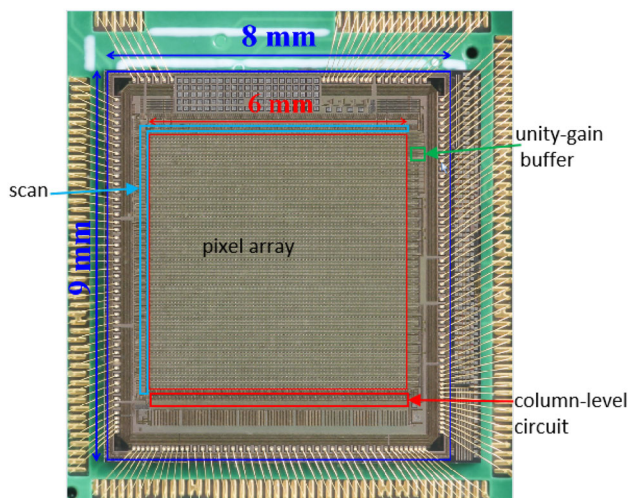
Fig. 9 (Color online) Layout of the Topmetal-CEE sensor

Fig. 13 (Color online) Photograph of the Topmetal-II- sensor

a high level. Therefore, a clock-cycle pulse of MAR-KER_S (the flag of the first pixel) was output at the 80th clock cycle. Each pixel is read out during one clock cycle. The pixels are read out successively when the speak signal

Fig. 14 (Color online) Block diagram of the readout electronics for the prototype beam monitor

is high. The scan module returns to select the first pixel when START_S is flipped from a low level to a high level, and SPEAK_S is high. The scan module stops scanning when the SPEAK_S is low. Therefore, we can set the number of pixels to be read by changing the timing of START_S or SPEAK_S. For example, the first 75 pixels were read using the timing shown in Fig. 12, respectively.

The photograph of the Topmetal-II- sensor is shown in Fig. 13. The total size of the sensor is 8 mm × 9 mm. The sensitive area is approximately 6 mm × 6 mm.

A block diagram of the readout electronics of the prototype beam monitor is presented in Fig. 14. It is composed of a data acquisition system (DAQ) and front-end and back-end electronics. In each direction, the front-end electronics consisted of a daughter board carrying four Topmetal-II- sensors through bonding wires and a mother board. The back-end board is composed of two readout boards, and a clock and synchronous board that provides the clock and synchronous signal for the readout board. The data received from the X- and Y-directions were transmitted to a PC through the DAQ.

2.3 Expected performance

Two baseline gas mixtures, Ar-CH$_4$ (90:10) and Ar-CO$_2$ (70:30), by volume, were considered for the detector. They are similar in terms of the number of electron–ion pairs per unit length generated by the traversing charged particles; however, they strongly differ with respect to the velocity and diffusion of the drifting electrons and resilience of the drift orientation to the magnetic field. Figure 15 shows the electron drift velocity, diffusion, and the effect on the drift orientation due to a magnetic field of 0.04 Tesla which is typical in the magnetic shield in the CEE, calculated by Garfield++ [26] and Magboltz [27, 28]. The baseline drift fields are 100 V/cm and 300 V/cm. Table 1 shows the gas properties of the two gas mixtures in the two drift fields. This shows that the Ar-CH$_4$ (90:10) gas mixture yields a considerably faster electron drift velocity, hence a smaller effect on the signal peaking time even considering its larger longitudinal diffusion. However, the Ar-CO$_2$ (70:30) gas mixture yields a smaller diffusion, and hence a better position resolution. Additionally, the electron drift orientation in Ar-CO$_2$ (70:30) is less affected by the magnetic field, which is an attractive property for application in the CEE.

To assess the impact of the residual magnetic field inside the magnetic shield on the position determination, the AvalancheMC method in Garfield++ was used to simulate electron trajectories in the presence of both electric and magnetic fields. The CEE magnet team calculates the magnetic field map. It has a typical magnitude of a few hundred gauss, roughly in the Y direction, but with
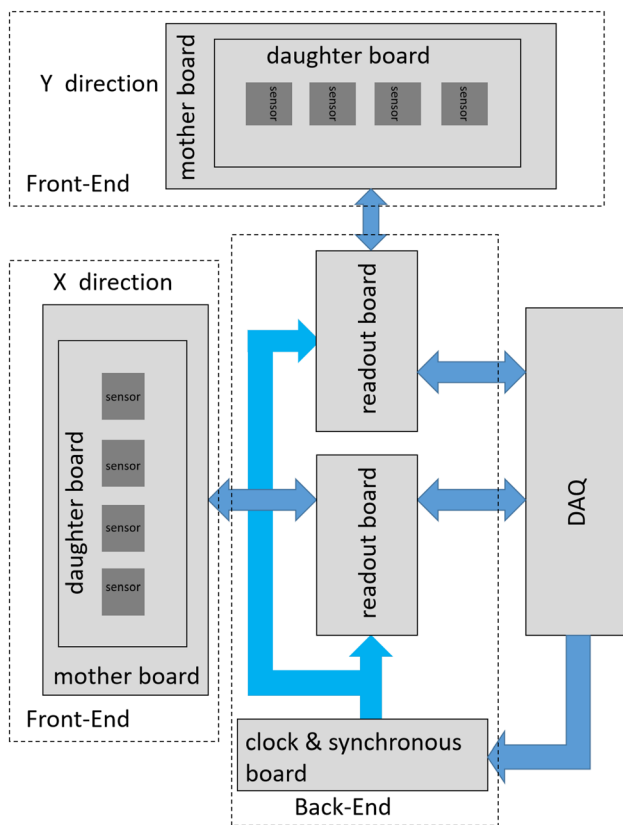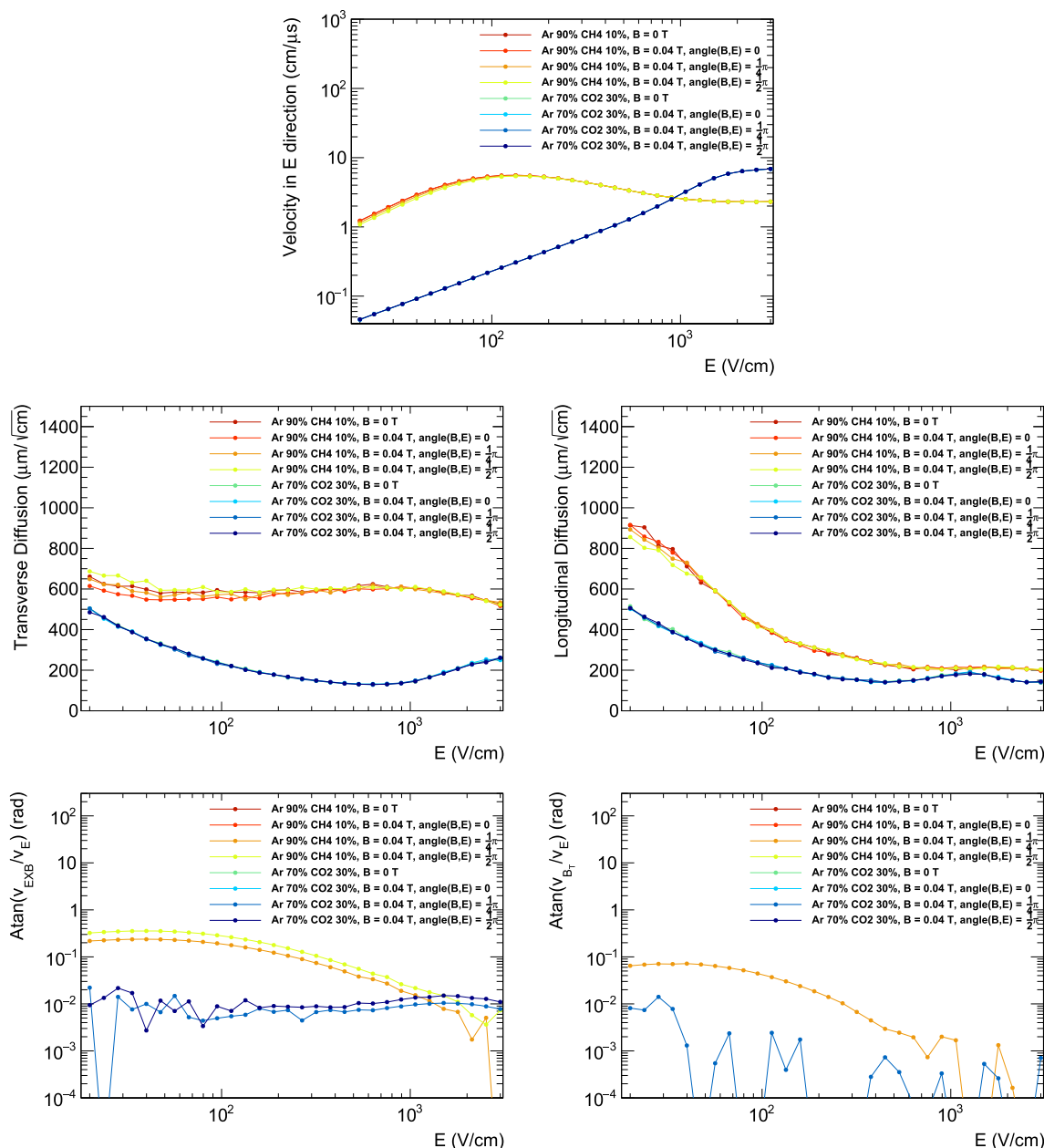
Fig. 15 (Color online) Gas properties as a function of the electric field strength calculated by Garfield++ and Magboltz. (Top) drift velocity in E direction; (middle left) transverse diffusion coefficient (middle right) longitudinal diffusion coefficient; (bottom left) velocity orientation owing to $V_{E \times B}$; (bottom right) velocity orientation owing to the V_B. Two types of gases, Ar-CH$_4$ (90:10) and Ar-CO$_2$ (70:30), are shown. For each gas, various magnetic field configurations are plotted: without a magnetic field, $B = 0.04$ T and parallel E, $B = 0.04$ T and is orthogonal to E, $B = 0.04$ T and the angle between B and E is $0.25\ \pi$

non-negligible X and Z components of strength up to approximately 100 gauss. Figure 16 shows the deviation of the calculated position from the true position of the beam, as a function of the beam vertical position, with a magnetic field at one candidate location and a uniform electric field of 300 V/cm. Within the vertical position of ± 1.5 cm, the variation in the deviation was within 10 μm for both field cages.

The expected spatial resolutions of heavy ions are calculated using pseudo-experiments. For a specified heavy-ion particle, the track is set as straight with uniform ionization, with the average energy loss calculated by Srim [29]. The pixel noise was represented by a Gaussian random number overlaying the nominal charge collection for each pixel. Table 2 lists the expected spatial resolutions of Xe at 780 MeV/u and U at 520 MeV/u for various

Table 1 Properties of gas mixtures at baseline drift fields calculated by Garfield++ and Magboltz

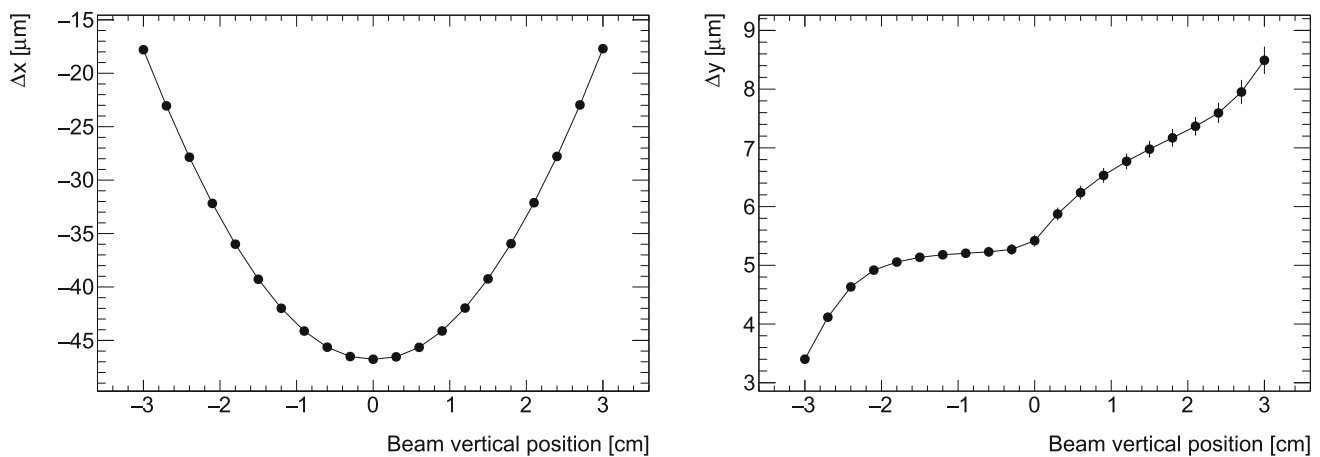| Drift field (V/cm)	Ar-CH$_4$ (90:10)		Ar-CO$_2$ (70:30)	
	100	300	100	300
$B -$ field $= 0$ T				
Drift velocity (cm/μs)	5.37	4.50	0.23	0.69
Transverse diffusion (μm/cm$^{1/2}$)	591	591	236	151
Longitudinal diffusion				
(μm/cm$^{1/2}$)	411	265	232	156
(ns/cm$^{1/2}$)	7.7	5.9	100.9	22.6
$B -$ field $= 0.04$ T, angle$(B, E) = \frac{1}{4}\pi$				
arctan(v_{EXB}/v_E) (rad)	0.189	0.080	0.005	0.006
arctan(v_B/v_E) (rad)	0.042	0.008	<0.005	<0.005

Fig. 16 Deviation of the calculated position from the true position of the beam, as a function of the beam vertical position, for the field cage measuring the X (left) and Y coordinates (right), respectively. The vertical direction points from the anode to cathode, and the origin is at the center of each field cage. The beam was assumed to be perpendicular to the X–Y plane, and the horizontal position (coordinate to be measured) was fixed at 0 when scanning the vertical position. The electric field was set to be uniform with a strength of 300 V/cm pointing in the vertical direction. The magnetic field is one candidate location for the beam monitor inside the magnetic shield

Table 2 Expected spatial resolutions of Xe at 780 MeV/u and U at 520 MeV/u for various transverse diffusion coefficients and pixel noises, for a drift length of 4 cm

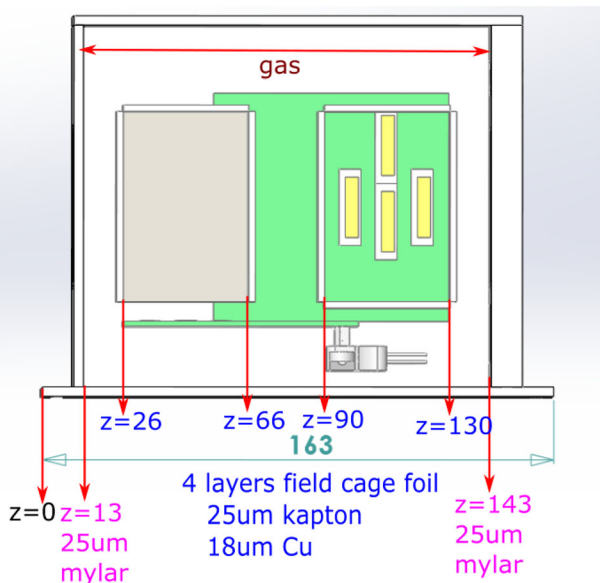| Diffusion coefficient (μm)	Pixel noise (e^-)	Spatial resolution (μm),	
		Xe	U
300	0	3.5	2.1
	50	13.2	5.3
	70	18.1	6.8
	100	25.3	10.0
600	0	6.5	3.9
	50	14.3	6.0
	70	18.9	7.8
	100	26.1	10.1

Fig. 17 (Color online) Materials of the beam monitor along the beam direction

transverse diffusion coefficients and pixel noises, for a drift length of 4 cm. The expected spatial resolution was less than 30 μm, even under a conservative pixel noise of 100 e^-.

To minimize the interference of the beam monitor with the beam, the materials that the beam particles traverse are carefully chosen. As shown in Fig. 17, the entrance and exit windows of the vessel are Mylar films with a thickness of 25 μm. The field strips were made of 18 μm-thick copper strips on top of a 25 μm-thick Kapton film. The energy loss by U at 520 MeV/u traversing the beam monitor averages 7.2 MeV/u, satisfying the explicit requirement of less than 10 MeV/u by CEE collaboration.

3 Performance with ^{241}Am α source

The prototype of the beam monitor was tested using a ^{241}Am α source in the laboratory. Figure 18 shows the photographs of the instruments for the prototype test. The gas used was Ar-CO_2 (70:30) because of its relatively small diffusion level. The electric field was set as 300 V/cm. The α source was placed inside the field cage adhering to the short side.

3.1 Spatial resolution

To assess the spatial resolution for a column or row of pixels, the Topmetal-II- sensor is configured to operate under the matrix-scan mode. A typical α trajectory, recorded using a single chip, is shown in Fig. 19 (top panel)


Fig. 18 (Color online) Photographs of instruments for the prototype test with ^{241}Am α source. Overall setup of the test (top); side view of the field cage (bottom left); top view of the field cage and motherboard, where a ^{241}Am α source is also observed (bottom right)

with pedestal subtraction applied pixel by pixel. The background noise is approximately 10–20 ADC counts per pixel. One ADC count equals 0.061 mV and is approximately two e^-. Gaus (μ, σ) fitting was applied to determine the α position in each column. The μ parameter represents the α position and is allowed to float during the fitting. The σ parameter represents the width of the distribution, which mainly stems from the transverse diffusion of the drifting charges, and is constrained to a size of 1–3 pixels. Figure 19 (middle and bottom) shows the pixel amplitude distributions in columns 0, 20, 40, and 60 and the corresponding Gaussian fits.

With the α positions in all 72 columns determined, the track was obtained by fitting a straight line to these positions, as shown in Fig. 20. The uncertainty of each position varies and is calculated by Gaussian fitting, with a larger uncertainty generally corresponding to vague signals. The residuals were calculated with respect to the fitted α track and are shown in Fig. 21. A Gaussian fit to the residuals yields $\mu = -2.78 \pm 4.69$ and $\sigma = 39.76 \pm 3.31$, which are consistent with the mean and standard deviation of the samples, respectively.

Fig. 19 (Color online) Signals of a typical α trajectory in one chip (top); pixel amplitude distributions in columns 0, 20, 40, and 60 and the corresponding Gaussian fits (middle and bottom)
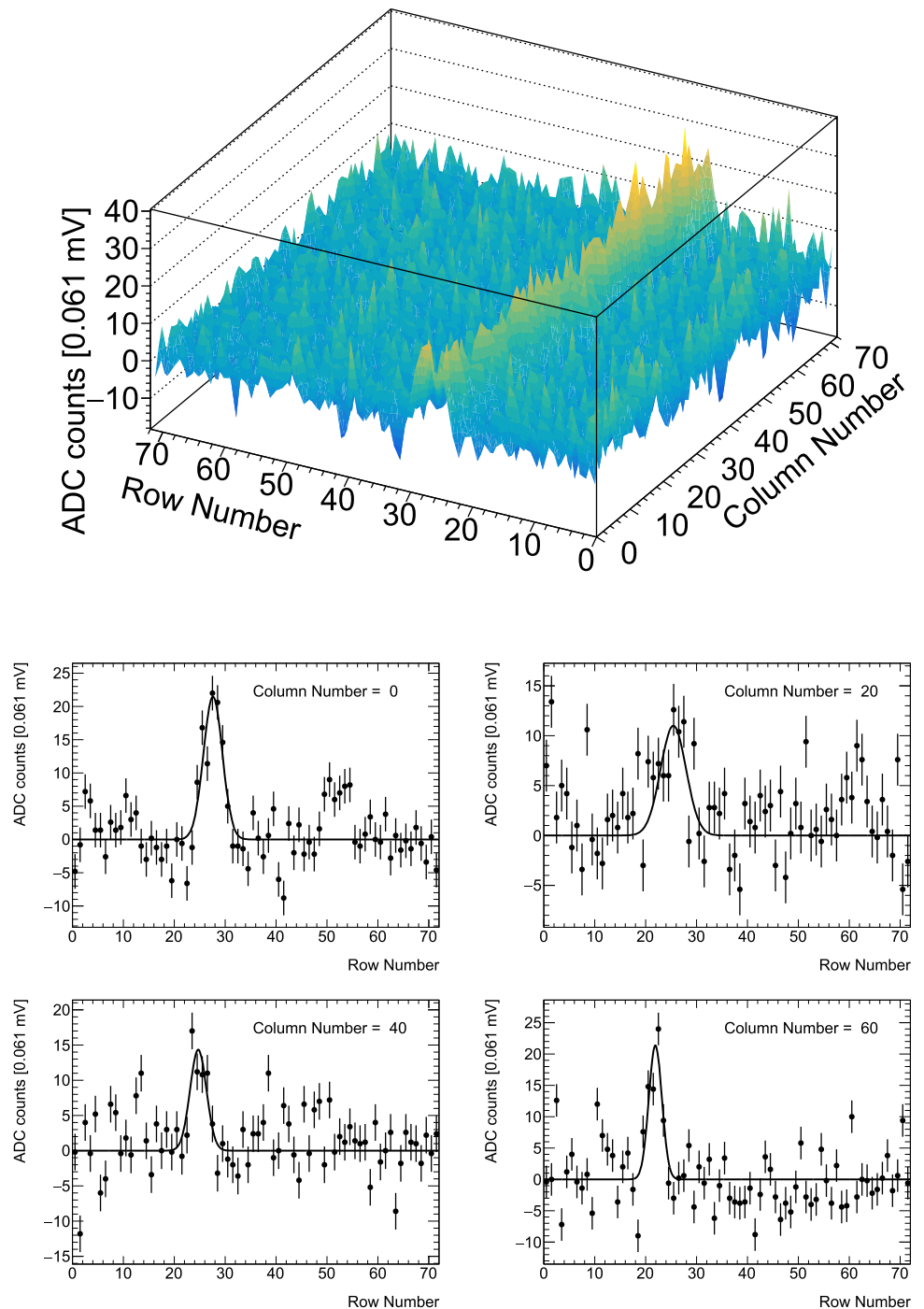
3.2 Time resolution

To evaluate the timing capability of the pixels, the Topmetal-II- chip was configured to scan only the first row. With the per-pixel scanning rate of 25 MHz, the time taken to scan a row of 72 pixels is 2.88 μs, effectively turning the chip into a waveform sampler for a row of pixels. The timing and amplitude information can then be calculated from the waveforms of individual pixels.

3.2.1 Time resolution of injected signals

In this study, a square signal with a frequency of 5 kHz and amplitude of 20 mV was injected into the pixels via guard ring capacitance. Figure 22 shows the output
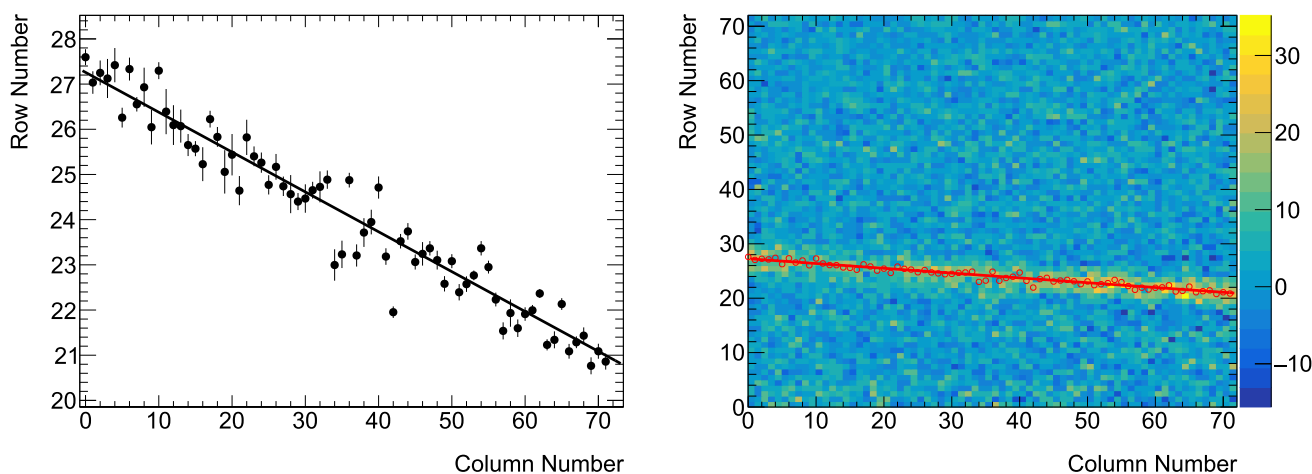
Fig. 20 (Color online) α position in each column obtained from the Gaussian fit and the fitted α track as a straight line (left); the same plot overlaid with the 2D plot of the pixel amplitudes of the chip (right)
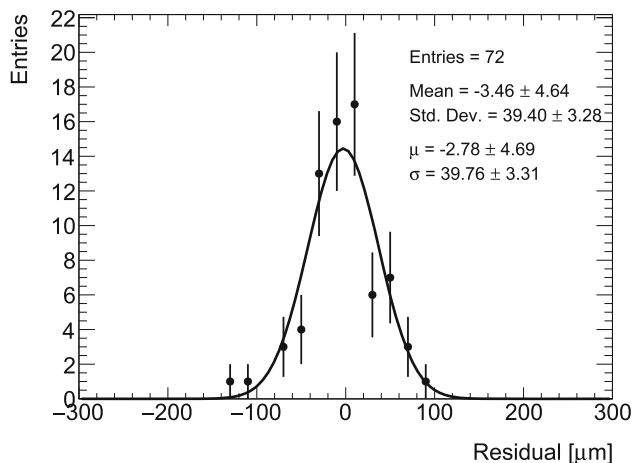

Fig. 21 Residual distribution of the α position in each column

waveforms of pixels 10–18 in one chip. The peaking time is approximately 2 to 3 μs. Because of the variations of the device and interconnection of parameters in the fabrication steps, the decay time constant varied from a few μs to approximately 20 μs for different pixels. In the Topmetal-II- sensor, the decay time is adjusted via a global DAC, and correction for pixel-to-pixel variations is impossible. In the Topmetal-CEE sensor, each pixel has a local integrated DAC, which can be tuned to correct for the decay time, thereby reducing the process variations.

The timing of the signal is determined by the rising edge of the signal waveform. The ADC time bin had a width of 40 ns, and the time interval between adjacent sampling points was 72 ADC time bins. To determine the timing of the signal, the base and peak of the rising edge were determined, and then the amplitude of the medium point of the rising edge was calculated. The corresponding ADC

time bin of this medium point was then determined using the interpolation method and was regarded as the timing of the signal. Figure 23 shows the distributions of the time measurements by the first row of pixels on the timings of six positive injected signals in Fig. 22. The standard deviation varied from approximately 500 to 650 ns for these six distributions, with an average standard deviation of 563 ± 17 ns.

The time resolution of the individual pixels can be determined by measuring the period of the injected signals. Because the period is calculated by the timing difference of the adjacent signals, the uncertainty of the period measurement is larger than that of the timing measurement by a factor of $\sqrt{2}$. Figure 24 shows the standard deviations of the five period measurements by individual pixels of the first row on the injected signals in Fig. 22. With an average value of 850 ± 26 ns, it translates to 601 ± 18 ns for the time resolution of the signal, which is consistent with the results of the other method mentioned above.

3.2.2 Time resolution of α signals

The time resolution has also been evaluated with α signals. Figure 25 shows the output waveforms of approximately 650 μs time duration of the same pixels as in Fig. 22, with obvious α signals on pixels 12–16 observed at approximately 80 μs (2000 ADC time bins). A local background fluctuation of approximately 10 ADC counts and drifting baseline were also observed for the pixels. The peaking time of the α signal is similar to that of the injected pulse signal, indicating a negligible contribution from the charge sensing process, that is, the combined effect of the electron drift velocity, CCE size, and longitudinal diffusion, which is expected from the numbers in Table 1.
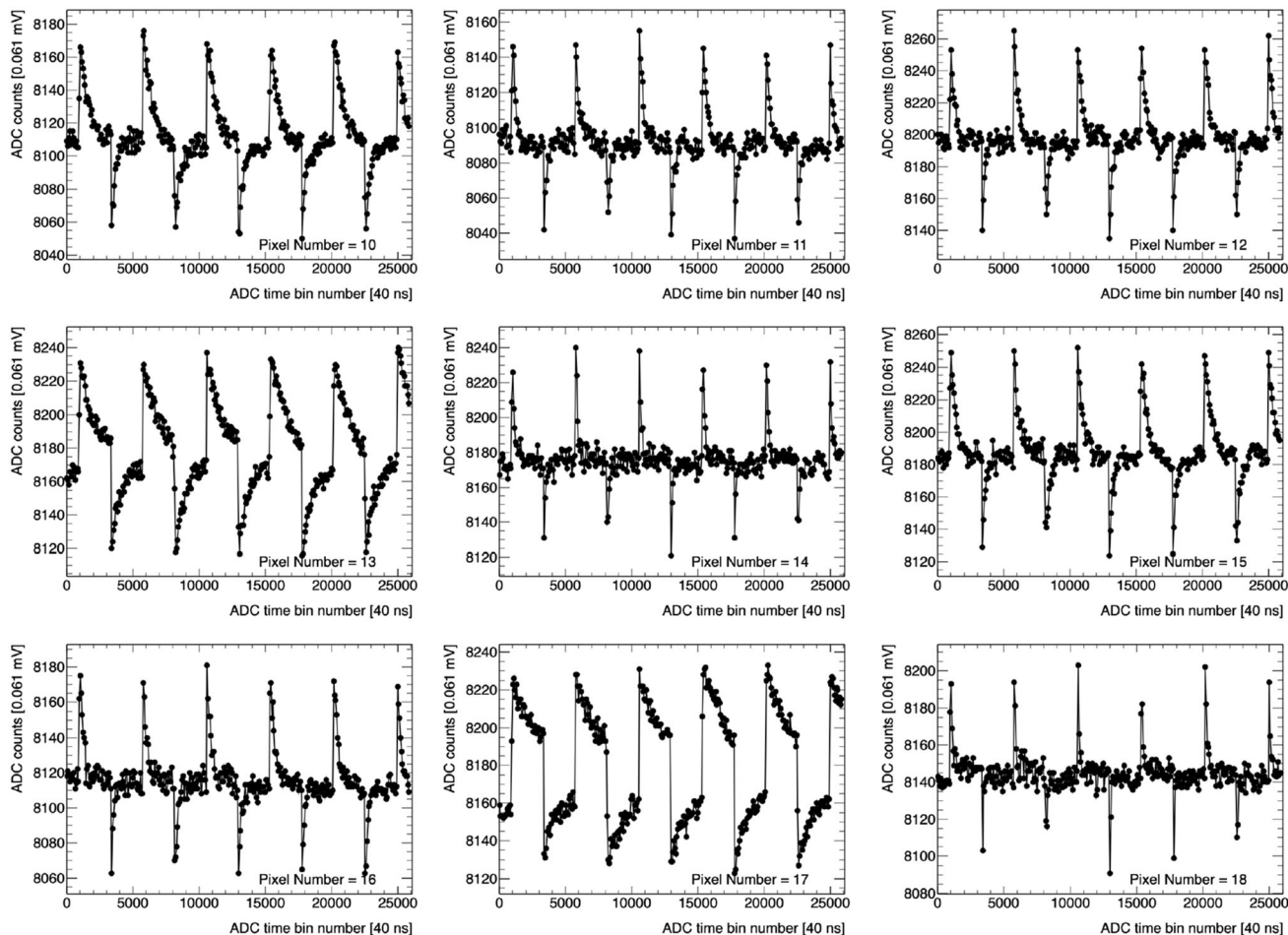
Fig. 22 Output waveforms of pixels 10–18 in one chip with injected square signal of 5 kHz frequency and 20 mV amplitude
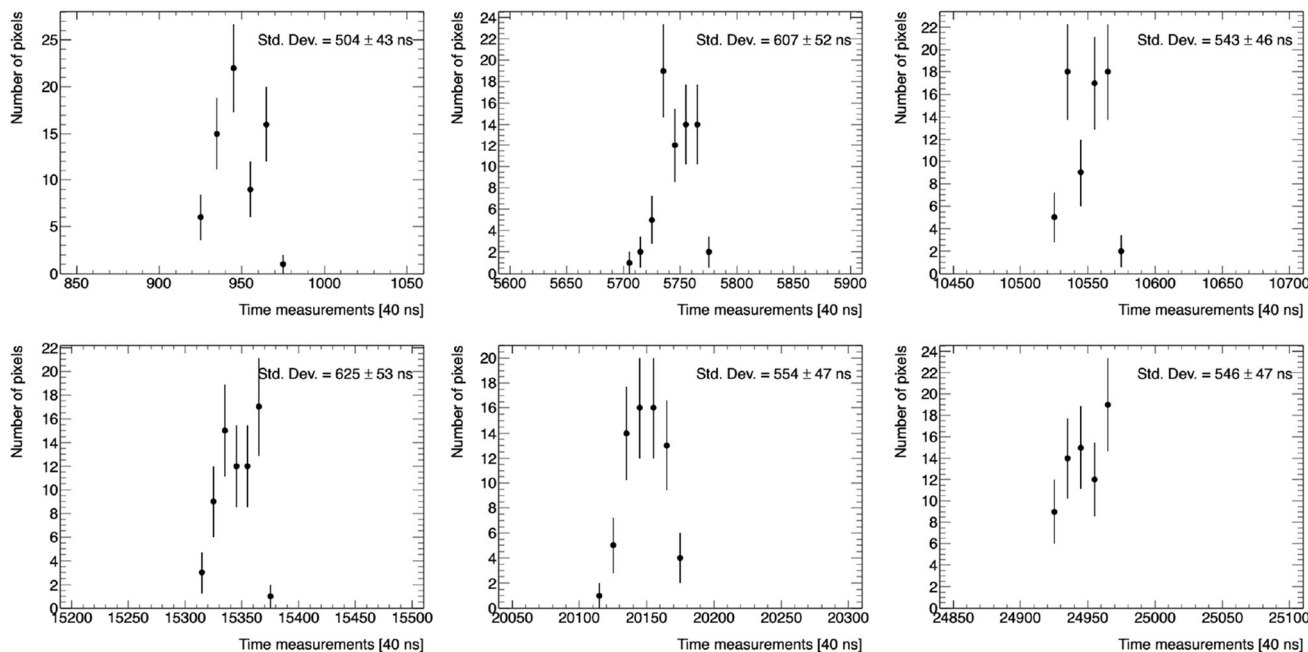

Fig. 23 Distributions of time measurements by the first row of pixels on the timings of the six positive injected signals as in Fig. 22
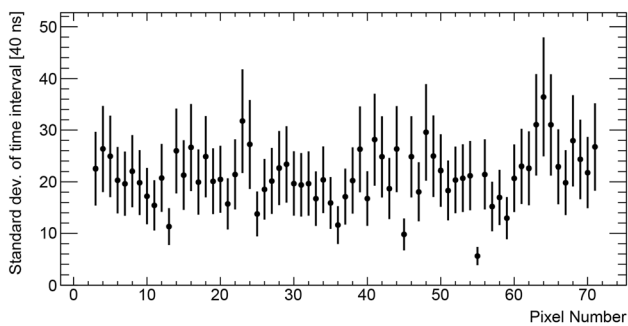
Fig. 24 Standard deviations of the six period measurements by individual pixels of the first row on the injected signals as in Fig. 22

The timing of the α signal determined by these five pixels is shown in Fig. 26 (left), with a standard deviation of 547 ± 173 ns, which was consistent with the results of the injected signals. The amplitude measurements are shown in Fig. 26 (right).

4 Conclusion

A prototype gaseous beam monitor was developed for the CEE spectrometer at HIRFL. A charge-sensing and readout sensor, named Topmetal-CEE, was specifically designed for beam monitoring and is currently under fabrication. The Topmetal-II- sensor, which has been developed for broader applications and shares great similarities with Topmetal-CEE, was used in the current prototype to demonstrate the working principle of the beam monitor. The prototype was tested by ^{241}Am α source in the laboratory. Typical events have a spatial resolution of less than 40 μm and a time resolution of less than 600 ns. With a
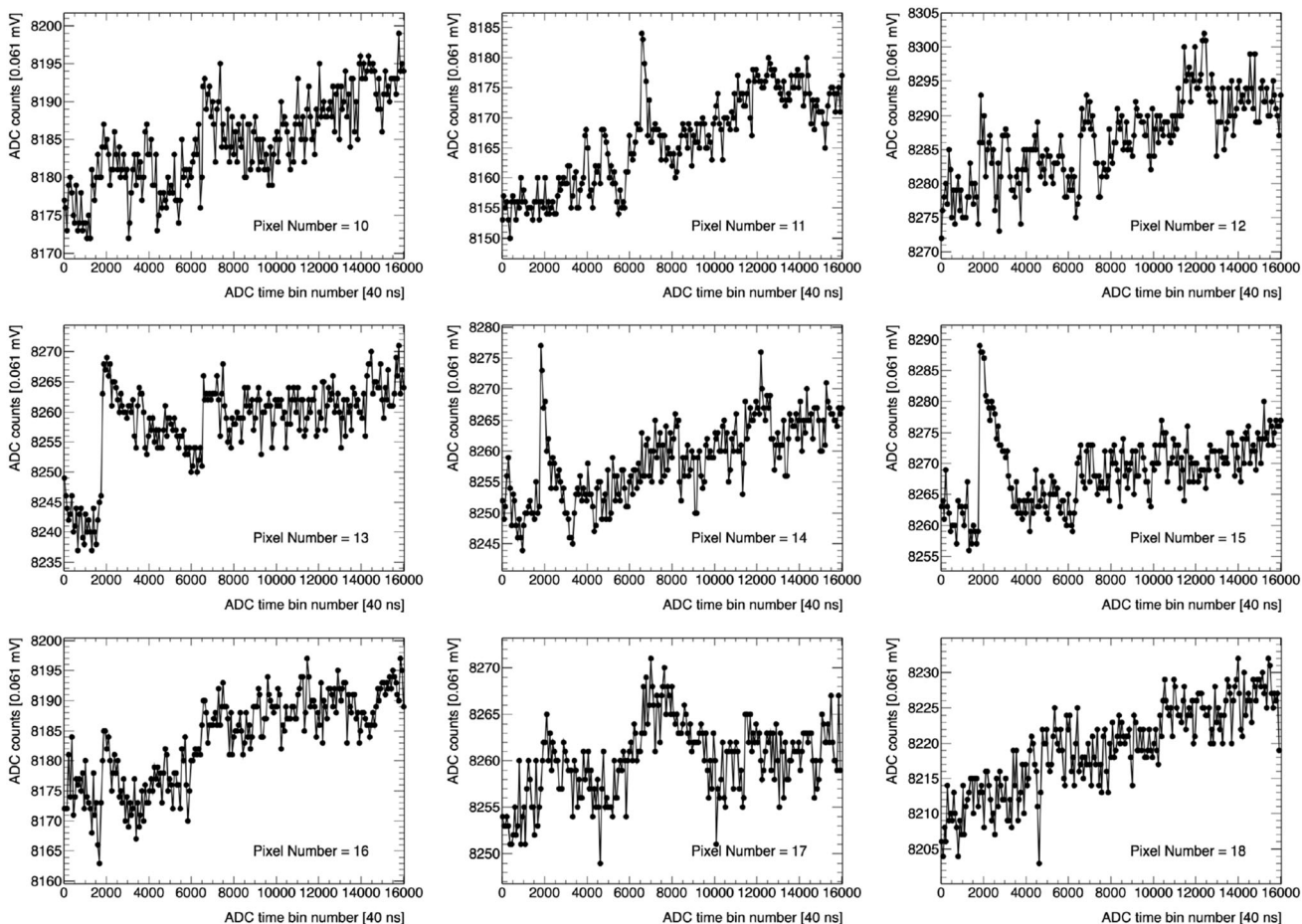

Fig. 25 Output waveforms of pixels 10–18 in one chip with obvious α signals on pixels 12–16 at approximately 80 μs (2000 ADC time bin)
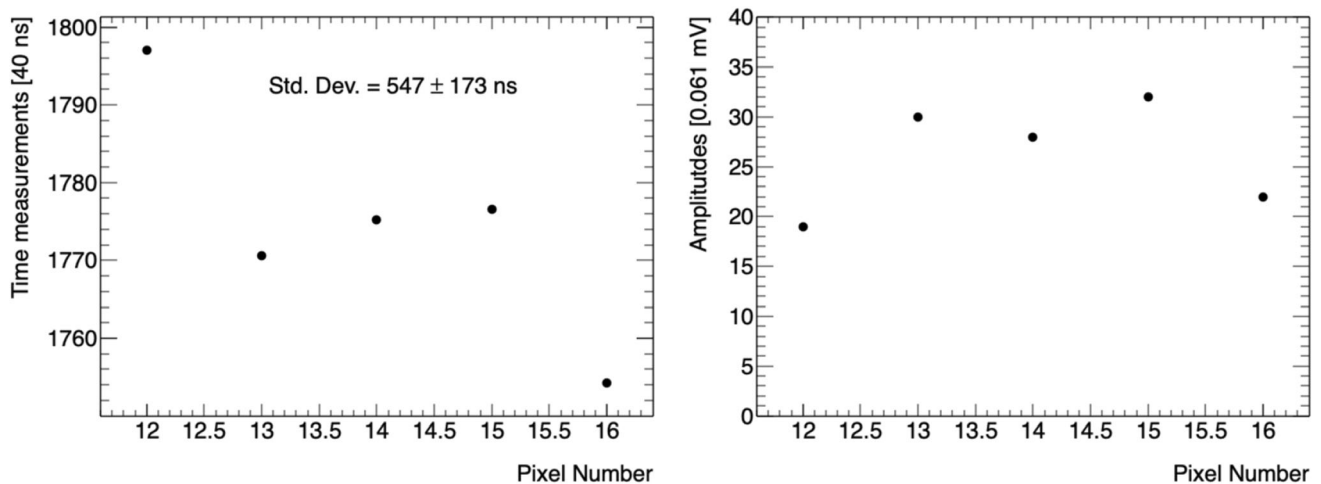
Fig. 26 Time measurements (left) and amplitude measurements (right) by pixels 12–16 on the α signals in Fig. 25

peaking time of approximately 2–3 µs and a decay time constant of approximately a few to 20 µs, the prototype is expected to withstand a beam rate of approximately 0.1 MHz, and a few times more considering the expected beam width of approximately a few millimeters and sub-millimeter transverse diffusion. For the Topmetal-CEE sensor, among the major improvements oriented toward the CEE beam monitor, the peaking time was reduced to approximately 100 ns, and the decay time constant was less than 900 ns, according to the simulation results. Therefore, it is anticipated that the upgraded prototype based on the Topmetal-CEE sensor could work well under a beam rate of 1 MHz with some redundancy. More detailed and systematic studies of the prototype, as well as studies of the upgraded prototype based on the Topmetal-CEE sensor, will be available soon.

References

1. L. Lü, H. Yi, Z. Xiao et al., Conceptual design of the HIRFL-CSR external-target experiment. Sci. China Phys. Mech. Astron. **60**, 012021 (2016). https://doi.org/10.1007/s11433-016-0342-x

2. J. Xia, W. Zhan, B. Wei et al., The heavy ion cooler-storage-ring project (HIRFL-CSR) at Lanzhou. Nucl. Instrum. Meth. A **488**, 11 (2002). https://doi.org/10.1016/S0168-9002(02)00475-8

3. Y. Yuan, J. Yang, J. Xia et al., Status of the HIRFL-CSR complex. Nucl. Instrum. Meth. B **317**, 214 (2013). https://doi.org/10.1016/j.nimb.2013.07.040

4. Z. Xiao, L.-W. Chen, F. Fu et al., Nuclear matter at a HIRFL-CSR energy regime. J. Phys. G Nucl. Part. Phys. **36**, 064040 (2009). https://doi.org/10.1088/0954-3899/36/6/064040

5. D. Hu, J. Lu, J. Zhou et al., Extensive beam test study of prototype MRPCS for the T0 detector at the CSR external-target experiment. Eur. Phys. J. C **80**, 282 (2020). https://doi.org/10.1140/epjc/s10052-020-7804-2

6. D. Hu, X. Wang, M. Shao et al., Beam test study of the MRPC-based T0 detector for the CEE. J. Instrum. **14**, C09030 (2019). https://doi.org/10.1088/1748-0221/14/09/c09030

7. D. Hu, M. Shao, Y. Sun et al., A T0/trigger detector for the external target experiment at CSR. J. Instrum. **12**, C06010 (2017). https://doi.org/10.1088/1748-0221/12/06/c06010

8. S. Zhu, H. Yang, H. Pei et al., Prototype design of readout electronics for zero degree calorimeter in the HIRFL-CSR external-target experiment. J. Instrum. **16**, P08014 (2021). https://doi.org/10.1088/1748-0221/16/08/p08014

9. W. Huang, F. Lu, H. Li et al., Laser test of the prototype of CEE time projection chamber. Nucl. Sci. Tech. **29**, 41 (2018). https://doi.org/10.1007/s41365-018-0382-4

10. L. He, Z. Song, L. Fei et al., Simulation of momentum resolution of the CEE-TPC in HIRFL. Nucl. Tech. **39**, 70401 (2016). https://doi.org/10.11889/j.0253-3219.2016.hjs.39.070401 (**in Chinese**)

11. S.-W. Tang, S.-T. Wang, L.-M. Duan et al., A tracking system for the external target facility of CSR. Nucl. Sci. Tech. **28**, 68 (2017). https://doi.org/10.1007/s41365-017-0217-8

12. H. Yi, Z. Zhang, Z.-G. Xiao et al., Prototype studies on the forward MWDC tracking array of the external target experiment at HIRFL-CSR. Chin. Phys. C **38**, 126002 (2014). https://doi.org/10.1088/1674-1137/38/12/126002

13. Y. Sun, Z. Sun, S. Wang et al., The drift chamber array at the external target facility in HIRFL-CSR. Nucl. Instrum. Methods A **894**, 72 (2018). https://doi.org/10.1016/j.nima.2018.03.044

14. L.-M. Lyu, H. Yi, L.-M. Duan et al., Simulation and prototype testing of multi-wire drift chamber arrays for the CEE. Nucl. Sci. Tech. **31**, 11 (2020). https://doi.org/10.1007/s41365-019-0716-x

15. Y. Fan, C. Gao, G. Huang et al., Development of a highly pixelated direct charge sensor, Topmetal-I, for ionizing radiation imaging. arXiv: 1407.3712

16. M. An, C. Chen, C. Gao et al., A low-noise CMOS pixel direct charge sensor, Topmetal-II-. Nucl. Instrum. Methods A **810**, 144 (2016). https://doi.org/10.1016/j.nima.2015.11.153

17. W. Ren, W. Zhou, B. You et al., Topmetal-M: A novel pixel sensor for compact tracking applications. Nucl. Instrum. Methods

A **981**, 164557 (2020). https://doi.org/10.1016/j.nima.2020.164557

18. J. Alme, Y. Andres, H. Appelshäuser et al., The ALICE TPC, a large 3-dimensional tracking device with fast readout for ultra-high multiplicity events. Nucl. Instrum. Methods A **622**, 316 (2010). https://doi.org/10.1016/j.nima.2010.04.042

19. "COMSOL—software for multiphysics simulation." https://cn.comsol.com/

20. P. Yang, G. Aglieri, C. Cavicchioli et al., Low-power priority address-encoder and reset-decoder data-driven readout for monolithic active pixel sensors for tracker system. Nucl. Instrum. Methods A **785**, 61 (2015). https://doi.org/10.1016/j.nima.2015.02.063

21. M. Liu, K. Lian, Y. Huang et al., A 12-bit 200 MS/s pipeline ADC with 91 mW power and 66 dB SNDR. Microelectron. J. **63**, 104 (2017). https://doi.org/10.1016/j.mejo.2017.03.006

22. S. Batchu, J.P. Talari, R. Nirlakalla, Analysis of low power and high speed phase frequency detectors for phase locked loop design. Proc. Comput. Sci. **57**, 1081 (2015). https://doi.org/10.1016/j.procs.2015.07.390

23. C. Gao, M. An, G. Huang et al., A low-noise charge-sensitive amplifier for gainless charge readout in high-pressure Gas TPC.

PoS **TWEPP2018**, 083 (2019). https://doi.org/10.22323/1.343.0083

24. G. Acconcia, M. Crotti, S. Antonioli et al., High performance time-to-amplitude converter array, in *2013 IEEE Nordic-Mediterranean Workshop on Time-to-Digital Converters (NoMe TDC)*, vol. 1 (2013). https://doi.org/10.1109/NoMeTDC.2013.6658229

25. W. Deng, W. Zhou, X. Sun et al., A high-precision coarse-fine time-to-digital converter with the analog-digital hybrid interpolation. IEICE Electron. Express **16**, 20181062 (2019). https://doi.org/10.1587/elex.16.20181062

26. H. Schindler, R. Veenhof, "Garfield++." http://garfieldpp.web.cern.ch/garfieldpp/

27. S. Biagi, "Magboltz." http://magboltz.web.cern.ch/magboltz/

28. S. Biagi, Monte Carlo simulation of electron drift and diffusion in counting gases under the influence of electric and magnetic fields. Nucl. Instrum. Meth. A **421**, 234 (1999). https://doi.org/10.1016/S0168-9002(98)01233-9

29. J.F. Ziegler, M. Ziegler, J. Biersack, SRIM—the stopping and range of ions in matter. Nucl. Instrum. Methods B **268**, 1818 (2010). https://doi.org/10.1016/j.nimb.2010.02.091